Combined Effect of Temperature Induced Strain and Oxygen Vacancy on Metal-Insulator Transition of VO₂ Colloidal Particles

Kargal L Gurunatha, Sanjayan Sathasivam, Jianwei Li, Mark Portnoi, Ivan P. Parkin,* and Ioannis Papakonstantinou*

Vanadium dioxide (VO₂) is a promising material in the development of thermal and electrically sensitive devices due to its first order reversible metal-insulator transition (MIT) at 68 °C. Such high MIT temperature (T_C) largely restricts its widespread application which could be enabled if a straightforward tuning mechanism were present. Here this need is addressed through a facile approach that uses the combined effects of temperature induced strain and oxygen vacancies in bulk VO₂ colloidal particles. A simple thermal annealing process under varying vacuum is used to achieve phase transformation of metastable VO₂(A) into VO₂(M2), (M2+M3), (M1) and higher valence V_6O_{13} phases. During this process, distinct multiple phase transitions including increased as well as suppressed T_C are observed with respect to the annealing temperature and varied amount of oxygen vacancies respectively. The latent heat of phase transition is also significantly improved upon thermal annealing by increasing the crystallinity of the samples. This work not only offers a facile route for selective phase transformation of VO₂ as well as to manipulate the phase transition temperature, but also contributes significantly to the understanding of the role played by oxygen vacancies and temperature induced stress on MIT which is essential for VO₂ based applications.

1. Introduction

Vanadium dioxide (VO₂) has attracted widespread attention as a promising energy-saving material due to its unique metal to insulator (MIT) transition at 68 °C and accompanying remarkable change in electronic and optical properties.[1,2] The structural phase transition from low temperature insulating phase (monoclinic M1) to high temperature metallic phase (rutile R) (**Figure 1**A) occurs at a critical temperature (T_C), resulting in an increase in resistance up to three to five orders of magnitude, as well as a significant change in optical constants in less than 500 fs.[3,4] For this reason, VO₂ has been applied across a wide range of applications; Mott transition field effect transistors (MTFET),[5,6] thermochromic smart windows,[7–9] biofouling,[10] micro actuators,[11] and temperature/gas/strain sensors.[12–14] In addition to the stable M1 and R phases, other vanadium polymorphs with widely varying length of V—O bonds, include VO₂(A), VO₂(B), VO₂(D), VO₂(P), VO₂(T), and VO₂(M2), which appear as intermediate phases or co-precipitates during the Hydrothermal synthesis.[15] More recently, a few of these metastable phases have been regarded as suitable precursors for synthesizing VO₂(M1) phase by high temperature calcination. For example, the thermal phase transformation of VO₂(D) to VO₂(R/M1), VO₂(B) to VO₂(R/M1), and VO₂(A) to VO₂(M1) was observed when the thermal annealing of the sample carried out under vacuum or under argon atmosphere.[16–19]

In order to realize the practical applications of VO₂ it is necessary to tune the T_C to the desired temperature and hence, several approaches have been employed such as external doping,[20] strain (mechanical strain, epitaxial strain, etc),[21] oxygen vacancies,[22] and hydrogenation.[23] Doping or substitution of V⁴⁺ with cations can either decrease (e.g., W⁶⁺, Nb⁵⁺, Ta⁶⁺, Mo⁶⁺) or increase (e.g., Ga³⁺, Al³⁺, Cr³⁺) the T_C depending on the incorporation of electrons or holes.[20] In some cases, doping metal ions were found to stabilize the intermediate insulating M2 and M3 phase (also called T phase) at room temperature,[24–26] yet this is rather restricted by the inhomogeneity of the elemental distribution. These intermediate phases also appear under compressive uniaxial strain along cR-axis in single crystal nanobeams[13,27–31] and upon epitaxial strain in granular thin-films.[32,33] The strain modulation of T_C and structural change

K. L Gurunatha, M. Portnoi, Prof. I. Papakonstantinou
Photonic Innovations Lab
Department of Electronic & Electrical Engineering
University College London
Torrington Place, London WC1E 7JE, UK
E-mail: i.papakonstantinou@ucl.ac.uk
S. Sathasivam, J. Li, Prof. I. P. Parkin
Department of Chemistry
University College London
20 Gordon st, London WC1H 0AJ, UK
E-mail: i.p.parkin@ucl.ac.uk

The ORCID identification number(s) for the author(s) of this article can be found under https://doi.org/10.1002/adfm.202005311.

2005311 (1 of 9)

**ADVANCED
SCIENCE NEWS**
www.advancedsciencenews.com
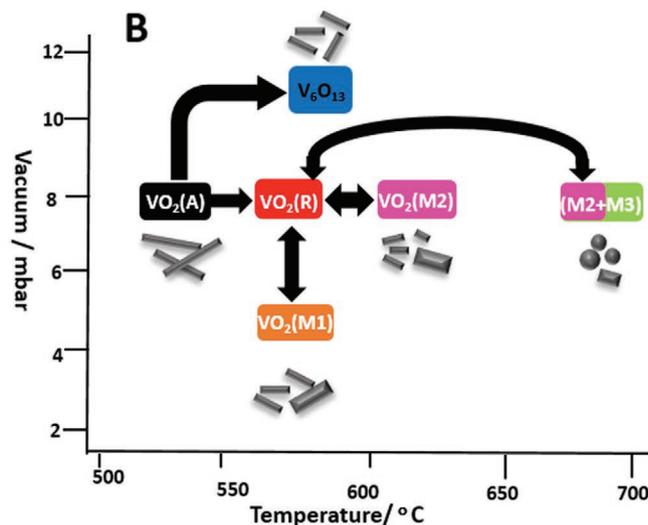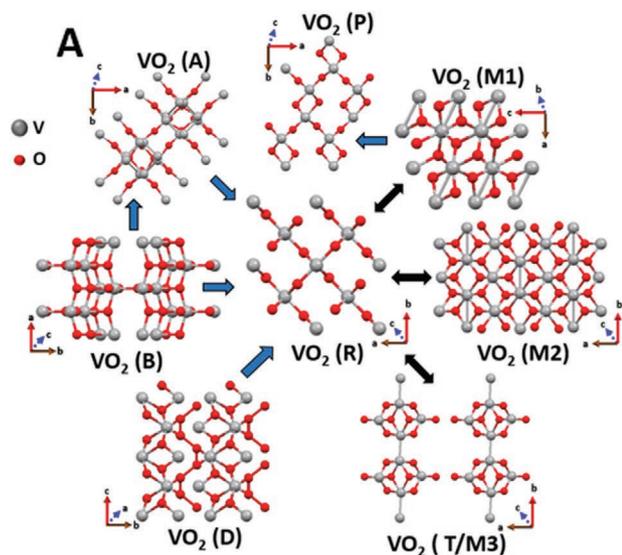
**ADVANCED
FUNCTIONAL
MATERIALS**
www.afm-journal.de

Figure 1. A) Structural comparison of different reversible and irreversible VO_2 phases. B) Schematic figure illustrating the phase transformation of $VO_2(A)$ into V_6O_{13}, $VO_2(M2)$, (M2+M3), and (M1) phases and morphology at different vacuum and different annealing temperature.

are closely associated with the change in length of cR-axis (adjacent V–V distance) of VO_2. Compressive strain along cR-axis in VO_2 nanobeams stabilize the $VO_2(R)$ phase by overlapping of d-orbitals leading to reduction of T_C, while the tensile strain elevates the T_C.[34] Similarly, epitaxial stress on VO_2 film samples grown on $TiO_2(001)$ and (110) substrate show suppressed and increased T_C with the shortened and elongated cR-axis, respectively.[35] It was observed that structural transition from M1 to R effectively shrinks the specimen while the transition from M1 to M2 expands it along cR-axis.[26] One can notice the significant differences in the arrangement of V-atoms in these phases (Figure 1A) where all the vanadium chains are straight and periodic at high temperature R-phase while, they dimerize and tilt along cR-axis on turning to M1 phase.[36,37] In the M2 phase, only one set of V-chains dimerize without tilt, while the nearest neighbor tilt away from the cR-axis without pairing but still found to be more insulating than the M1 phase.[3,38] In the intermediate triclinic T phase (also called M3 phase), pairing on one set of vanadium chains has been reported to be twisted slightly.[35] Recently, the M2 phase has attracted a great attention as a key element in understanding the transition mechanism between M1 and R phases but also because it is regarded as a true Mott insulator,[39] where MIT is free of any structural change. The M2 or M3 phase stabilization in granular films is strictly thickness-dependent, where strain relaxation in thicker films is evident in their MIT properties.[40] Therefore, intermediate phase stabilization in single crystalline VO_2 particles can be superior in thin-films, owing to their better conductivity due to lack of grain boundaries and fewer defects.

Another powerful strategy to alter T_C is to control the amount of electron donors such as oxygen vacancies. When a small amount of such vacancies are present, not only is it possible to elicit significant reduction to T_C, but also the electrical and chemical properties of VO_2 can be tuned.[22,41] For example, ionic liquid electrolyte gating was shown to substantially alter the properties of VO_2 thin films by metallization of insulating phase with the introduction of oxygen carriers.[5] Jeong

et al. reported the suppression of MIT temperature and stabilization of metallic phase below 5 kelvin by electrolyte gating of epitaxially grown VO_2 thin-films on TiO_2 and Al_2O_3 single crystal substrates.[22] However, electrochemical reaction with an ionic liquid tends to damage the crystallinity of VO_2 over time. In contrast, increase in T_C of MIT was recorded with increase in oxygen content for VO_2 thin-film samples grown under different oxygen exposure by Basu et al.,[42] found increased amount of V (with excess oxygen content) revealing the crucial importance of oxygen concentration during the annealing. Aside from this, regular interconnected nanonets composed of VO_2 nanorods grown on c-cut sapphire,[43] was also reported and showed varying resistance with respect to the different oxygen vacancy concentration.[41] These works indicate VO_2 has specific tolerance for oxygen vacancies despite the several complex $V_nO_{2n\pm1}$ compounds (V_2O_3, V_4O_7, V_5O_9, V_2O_5, V_3O_7, V_6O_{13}, etc). However, a clear understanding of the role of oxygen vacancies in the phase stability of VO_2 is still lacking. Therefore, a convenient and effective technique needs to be established to quantitatively induce strain as well as oxygen vacancies in VO_2 samples in order to exemplify their role on MIT.

In this work, we report the combined effect of temperature induced strain and oxygen vacancy on MIT during the metastable phase transformation of hydrothermally synthesized $VO_2(A)$ microrods. Specifically, sequence of vanadium oxide phases; V_6O_{13}, VO_2–(M2), (M2+M3), and (M1) were obtained by simple thermal annealing of colloidal $VO_2(A)$ microrods at different vacuum levels (Figure 1B). Compare to the previous works, we establish the critical role of varied vacuum during the thermal annealing resulting in the formation of different vanadium oxide phases. Multiple increased and suppressed metal–insulator transition was observed simultaneously for the first time in colloidal particles and attributed to the formation of $VO_2(M2/M3)$ phases and oxygen vacancies which are further explained. This technique not only helps in transformation and stabilization of the bulk metastable phase into the desired insulating phase but also facilitates the research on the role of
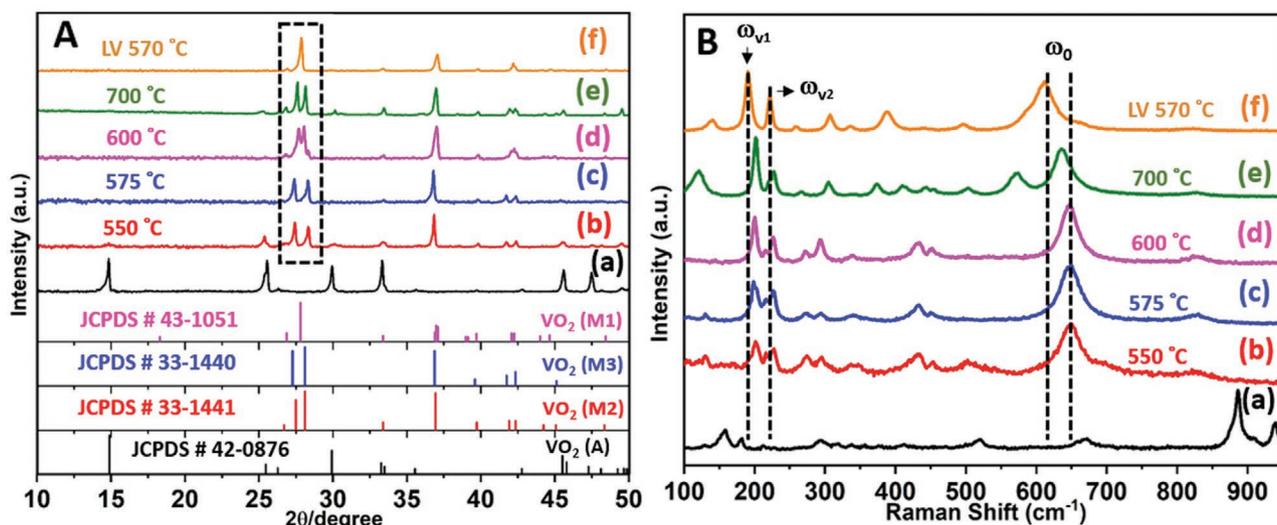
ADVANCED
SCIENCE NEWS
www.advancedsciencenews.com

ADVANCED
FUNCTIONAL
MATERIALS
www.afm-journal.de

Figure 2. A) Standard X-ray diffraction (XRD) pattern in JCPDS plots of VO₂(A), VO₂(M2), VO₂(M3), VO₂(M1) followed by a) as-synthesized sample, annealed sample at b) 550 °C, c) 575 °C, d) 600 °C, e) 700 °C at vacuum 7–9 mbar, and f) sample annealed at 570 °C with low vacuum (4 mbar) LV-570 °C. B) Corresponding Raman spectra of as-synthesized and annealed samples. All the measurements were taken at room temperature after annealing sample at respective temperature.

oxygen vacancy and strain on the MIT of VO₂. Furthermore, bulk stabilization of VO₂(M2) phase in colloidal particles is also an important step toward practical realization of MTFET.

2. Results and Discussion

2.1. Synthesis of VO₂(A) Microrods, Morphology, and Structure

The process begins with the formation of VO_2^+, OH^-, and N_2H_4 complex by combining hydrolyzed precipitate from V_2O_5 with Hydrazine and further adjusting the pH through the addition of NaOH solution.[44] The reaction conditions such as pH, concentration, temperature, and addition of precise amount of surfactant (CTAB) during the formation of the precipitate were important factors in determining the phase, size, and shape of the final product. The addition of CTAB prior to the precipitation with NaOH and subsequent hydrothermal treatment results in the formation of phase pure VO₂(A) microrods. The phase composition and purity of the as-synthesized product were analyzed by powder X-ray diffraction (P-XRD) and Raman spectroscopy (**Figure 2**). All the diffraction peaks are sharp and can be readily assigned to the tetragonal crystalline phase (space group: p4/ncc) of VO₂(A), in very good agreement with the literature values (JCPDS card no. 42–0876) whose plots are shown in Figure 2A(a). Compared with the calculated XRD pattern, the strong intensity (110), (102), and (220) peaks at 14.8°, 25.5°, and 29.9° respectively indicate good crystallinity and high purity of the as-synthesized VO₂(A) phase (Figure 2A(a)). In addition to the phase purity, Raman spectra gave more detailed information about the local structure of VO₂(A) followed by phase evolution at different temperatures. Three types of Raman active modes were observed between 100–1100 cm⁻¹ for VO₂(A): i) The lattice modes at 159, 180, 212, 293 cm⁻¹, ii) the VO₆ Octahedra rotation modes at 412, 520, 667 cm⁻¹, and finally, iii) the antisymmetric

and symmetric stretching of octahedra and distorted square pyramids at 887, 940 cm⁻¹.[45,46] The detailed morphology, size, and microstructure of VO₂(A) products were characterized by SEM and TEM analysis (**Figure 3**). The low and high magnification SEM images (Figure 3A,B) show that as-synthesized sample composed of large and regular microrods of up to several tens of micro meters in length. Low and high resolution TEM (LRTEM and HRTEM) analysis of single nanorod (Figure 3C,D) revealed the consistent fringe spacing of 0.59 nm matches well with the (110) interplanar spacing of the metastable VO₂(A) phase.[47] The corresponding selected area electron diffraction pattern (Figure 3D inset) further proved the good crystallinity of the as-synthesized VO₂(A) microrods.

2.2. Thermal Phase Transformation of VO₂(A) Microrods

The phase transformation of VO₂(A) microrods was carried out in a furnace at 550–700 °C with a 4–12 mbar vacuum range for a duration of 2–3 h. At vacuum 10–12 mbar, thermal annealing of VO₂(A) at 550–600 °C resulted initially in the formation of V_6O_{13} phase as shown by P-XRD (Figure S1, Supporting information). When thermal annealing was carried out at 550 °C with slightly decreased vacuum (7–9 mbar), a different phase change was observed (Figure 2A(b)). The strong intensity (110), (102), and (220) peaks were minimized and new intense peaks appeared at 27.4°, 28.3°, and 36.8°, indicating the formation of new structural symmetry induced by temperature. With increasing annealing temperature, all the peaks corresponding to VO₂(A) phase were diminished and slight variation in the peak positions at 27.4° and 28.3° were observed (Figure 2A(c,d)). Analysis of the diffraction peak positions in these samples (575, 600 °C) revealed the formation of VO₂(M2) phase (space group: C2/m),[26] whereas diffraction peaks at 700 °C (Figure 2A(e)) showed mixed phase with some peaks
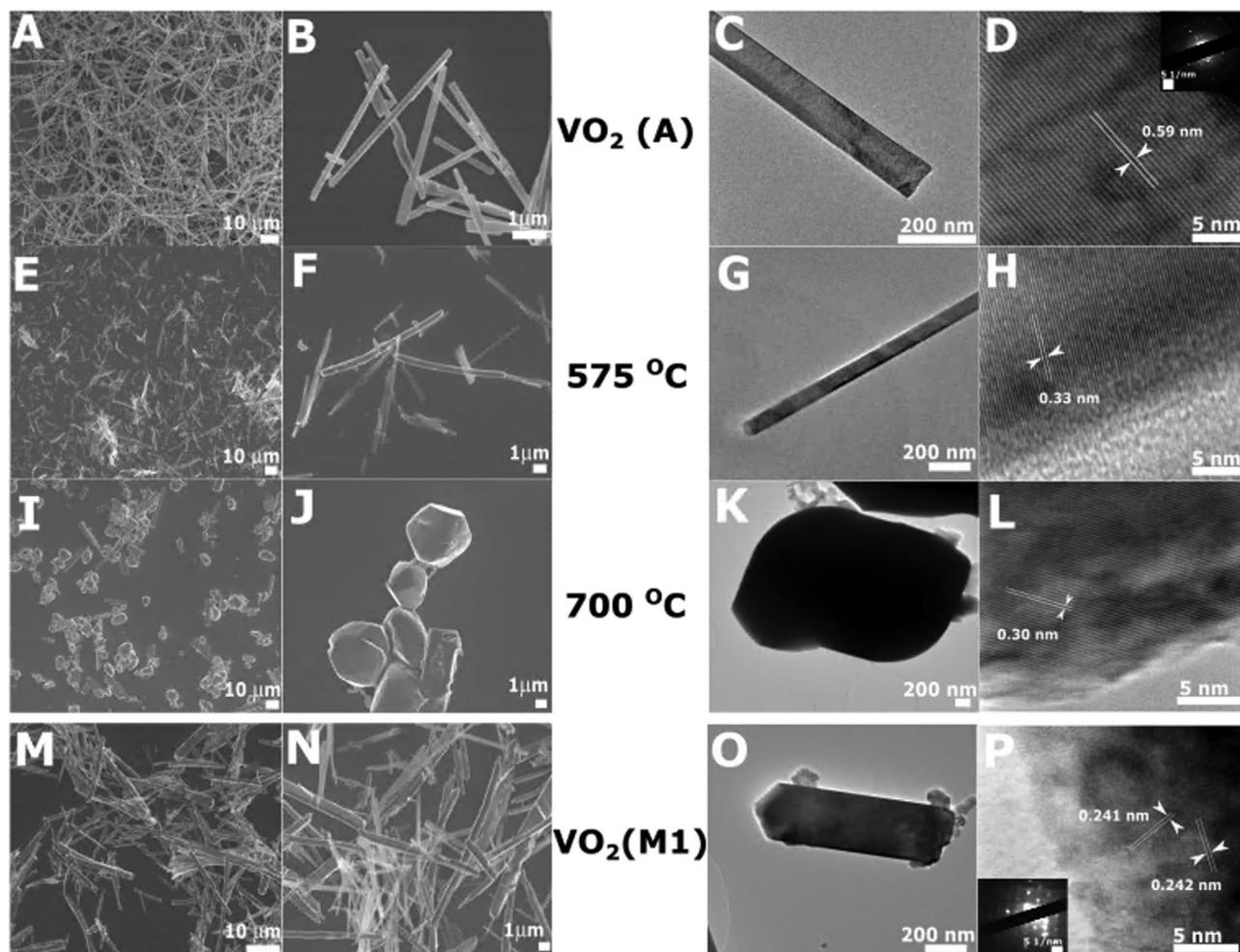
**ADVANCED
SCIENCE NEWS**

www.advancedsciencenews.com

**ADVANCED
FUNCTIONAL
MATERIALS**

www.afm-journal.de

Figure 3. Low and High magnification SEM and corresponding LRTEM, HRTEM images of A–D) as-synthesized $VO_2(A)$ microrods, E–H) sample annealed at 600 °C, I–L) sample annealed at 700 °C, and M–P) $VO_2(M1)$ sample.

indexed to $VO_2(M3)$ phase (space group: P2/m),[48] along with the former $VO_2(M2)$ phase. Annealing $VO_2(A)$ sample at 570 °C under low vacuum (4 mbar) led to the formation of pure monoclinic $VO_2(M1)$ phase (space group: P2/c),[49] indicating typical solid-state phase transformation.

Raman spectroscopy was also used to distinguish between the different VO_2 phases by analyzing Raman active modes. Several attempts were made previously to establish a phase diagram by using phonon frequency shift (ω_0) in M1, M2, M3, and R phases.[24,50–52] When the sample was annealed at 550 °C (Figure 2B(b)) all the peaks corresponding to $VO_2(A)$ phase disappeared and new peaks corresponding to the M2 phase were observed. The M2 Raman response can be readily distinguished by the dominant phonon frequency (ω_0) at 649 cm^{-1} which was related to V−O bonding and low-frequency phonons (ω_{V1}) at 201 cm^{-1}, followed by splitting (ω_{V2}) at 217, 226 cm^{-1} corresponding to V−V lattice motion. Additional phonon peaks were also observed at 130, 273, 293, 338, 432, 501, and 828 cm^{-1}.[46] The M2 phase appears to be stable despite an increase in annealing temperature to 600 °C (Figure 2B(c,d)). Slight blue shift and splitting in the ω_0 phonon was observed at 572 and 635 cm^{-1}, after annealing the sample at 700 °C. In addition to the specific change in the

ω_0 peak position, lower-frequency Raman modes also experience similar frequency shift. This phonon behavior is distinctive of the structural properties of the triclinic phase and substantiates the formation of the M3 phase. The Raman spectra of the sample annealed at 575 °C under vacuum below 4 mbar (Figure 2B(e)) show Raman modes at 142, 190, 221, 259, 307, 336, 388, 497, and 612 cm^{-1} and can be readily assigned with that of M1 phase as reported in the literature.[46,51]

To get a better insight on the phase transformation, we conducted in situ P-XRD by annealing the $VO_2(A)$ sample from 25–700 °C in a sealed micro quartz capillary tube under atmospheric pressure (See experimental details); the corresponding patterns are shown in **Figure 4**. $VO_2(A)$ is stable until 500 °C and phase transformation occurs between 525–550 °C. The P-XRD acquired at room temperature after cooling the sample, evidences the presence of $VO_2(M2)$ phase which confirms the irreversible phase transformation from $VO_2(A)$ to $VO_2(R)$ and reversible phase transformation from $VO_2(R)$ to $VO_2(M2)$. It is important to note here that the bulk stabilization of M2 phase at room temperature was achieved with gradual increase in annealing temperature, whereas (M1) phase transformation was observed only when thermal annealing was
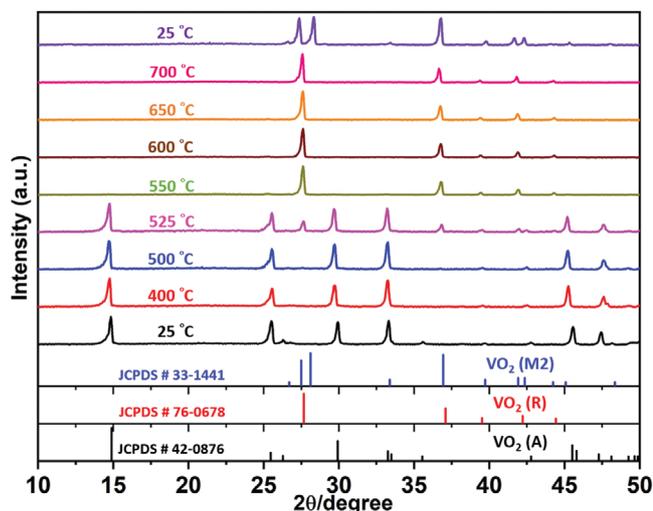
**ADVANCED
SCIENCE NEWS**

www.advancedsciencenews.com

**ADVANCED
FUNCTIONAL
MATERIALS**

www.afm-journal.de

Figure 4. In situ X-ray diffraction study of phase transformation process from VO$_2$(A) to VO$_2$(R) to VO$_2$(M2).

carried out at low vacuum (4 mbar). Few traces of (M3) phase also appeared at 700 °C in the XRD pattern, which was also evident in Raman spectra that showed both (M2) and (M3) phases co-exist at this temperature. The overall phase transformation sequence revealed from P-XRD and Raman was: VO$_2$(A)→VO$_2$(R)→VO$_2$(M2)→VO$_2$(M3) at vacuum 7–9 mbar whereas, at low vacuum (4 mbar): VO$_2$(A)→VO$_2$(R)→VO$_2$(M1). It appears that VO$_2$(M1) phase is thermodynamically stable product during the transformation from metastable VO$_2$(A) at low vacuum (4 mbar) whereas, VO$_2$(M2) and (M3) phases dominate when annealed at vacuum 7–9 mbar. The thermal annealing also induces change in the morphology of VO$_2$(A) where the sample at 600 °C shows broken microrods and significant reduction in its length and surface roughness (Figure 3E,F). Importantly, electron micrograph revealed well preserved crystallinity of the microrods with a fringe spacing of 0.33 nm, similar to the (011) plane spacing of VO$_2$(M1) phase,[53] (Figure 3G,H). Sample annealing at 700 °C resulted in the complete transformation of microrods to larger spheres of varying diameter 3–10 µm (Figure 3I–L) and reduced fringe spacing to 0.30 nm, possibly due to the increase in strain along a-axis (A_R) in addition to c-axis (C_R). The M1 phase transformation at low vacuum (4 mbar) (Figure 3M–P) showed preserved morphology with small amounts of fragmented microrods and measured lattice spacing 0.242 and 0.241 nm corresponding to (211) plane of the VO$_2$(M1) phase.

2.3. Elemental Composition of VO$_2$(A) and VO$_2$ Polymorphs

X-ray photoelectron spectroscopic (XPS) analysis was carried out on the as-synthesized VO$_2$ and annealed samples to determine the chemical composition and bonding states. The spectra were calibrated to the oxygen bound to V in the VO$_2$ lattice at 530.0 eV as proposed by Silversmit et al.[54] Although this approach is different to other XPS fitting which calibrates against adventitious carbon, several reports showed that O 1s signal is a better energy reference compared to the C 1s for V2p binding energy.[55,56] The XPS survey spectrum of VO$_2$(A)

and annealed samples clearly show only the expected peaks for elements of carbon (from inherent surface contamination), oxygen, and vanadium (Figure S2a, Supporting information) and no peaks of impurity elements. High-resolution scans of V2p and O 1s environments were collected and fit together by using a Shirley background and mixed Gaussian–Lorentzian (GL 30) peaks via Casa XPS software (**Figure 5**a). The V 2p peaks for all samples had asymmetrical line shape and were best fit with either two sets of doublets (for the VO$_2$(A), 550 °C annealed and VO$_2$(M1) samples) or three set of doublets (for the 575, 600, and 700 °C annealed VO$_2$ samples). The results are presented in **Table 1**. For all samples, a V2p$_{3/2}$ peak was seen between 517.3–517.6 eV and 515.5–516.2 eV corresponding to V(V) and V(IV), respectively.[54,57] For the 575, 600, and 700 °C annealed VO$_2$ samples, an additional V2p3/2 peak was seen between 514.6 and 515.0 eV for V(III).[58] The V(IV) to V(V) and V(IV) to V(III) ratios on the surface of the samples are also given in Table 1. For the VO$_2$(A) and VO$_2$(M1) samples the V(IV) to V(V) ratio were 1.5 and 1.7 respectively, that is, VO$_2$ rich, for 575 °C vacuum annealed sample the V(IV) and V(V) ratios were equal. The other samples were all V$_2$O$_5$ rich on the surface, presumably due to surface oxidation during annealing. X-ray fluorescence spectroscopy (XRF) was also performed with 10 ppm accuracy on the VO$_2$(A) and annealed sample (600 °C) to confirm sample purity. The spectra showed that aside from very small Fe (0.3 at%) detected from the sample holder, no impurities were present in the samples (Figure S3, Supporting Information). Therefore, formation of VO$_2$(M2) and M3 phase was a purely stress/strain induced effect and any form of elemental doping by impurities can be ruled out.

2.4. Thermal Analysis of VO$_2$ Polymorphs

The thermochromic phase transition temperature (T_C; $T_{C\text{-heat}}$ for insulator to metal, IMT and $T_{C\text{-cool}}$ for the metal-insulator transition, MIT) of as-synthesized VO$_2$(A) and annealed samples were investigated by differential scanning calorimetry (DSC) (**Figure 6**a). When the phase transition of VO$_2$(A) occurs, it exhibits noticeable endothermic peak at 161 °C due to conversion from low temperature phase (VO$_2$(A)$_{LTP}$—P4/ncc, 130) to high temperature phase (VO$_2$(A)$_{HTP}$—I4/m, 87),[59,60] but no reversible transition in the cooling cycle.[60] However, for the sample annealed at 550 °C (Figure 6b, Figure S4a, Supporting Information), the endothermic transition temperature ($T_{C1\text{-heat}}$) was centered at ≈66.8 °C with exothermic peak found at 58 °C ($T_{C1\text{-cool}}$). Further analysis of DSC curves by multiple peak fitting revealed an additional endothermic peak (Figure S4b, Supporting Information) observed at 70.5 °C ($T_{C2\text{-heat}}$) which dominates with increasing annealing temperature (575–700 °C) and also undergoes slight red shift (Figure S4c–e, Supporting Information). Interestingly, we noticed an additional lower transition temperature ($T_{C3\text{-heat}}$) at 44.7 °C for the 575 °C annealed sample (Figure S4c, Supporting Information). This peak in contrast, blue shift with increasing annealing temperature (575–700 °C, Figure S4c–e, Supporting Information) and further show splitting at 38.9 °C ($T_{C3\text{-heat}}$) and 34.1 °C ($T_{C4\text{-heat}}$) when annealed at 700 °C (Figure 6e and Figure S4e, Supporting Information). The exothermic profile shows reversible
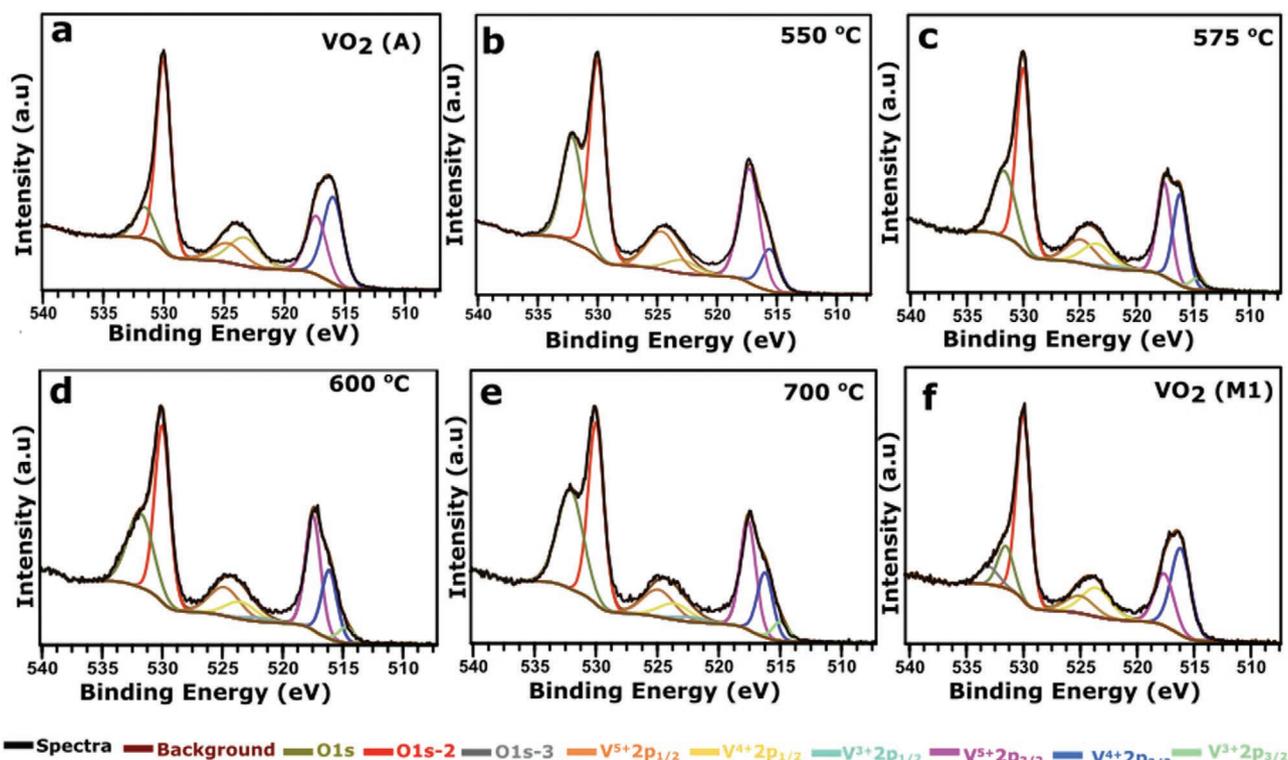
Figure 5. High resolution V2p$_{3/2}$ XPS spectra of a) VO$_2$(A) microrods, annealed sample at b) 550 °C, c) 575 °C, d) 600 °C, e) 700 °C, and f) VO$_2$(M). All the samples were cooled back to room temperature after annealing for XPS measurement.

transition temperature ($T_{C\text{-cool}}$) with multiple peaks observed in the sample with respect to their endothermic transition (Figure S5, Supporting Information). Sample VO$_2$(M1) (Figure 6f) show typical first order transition at 68.5 and 62.3 °C during the heating and cooling cycle respectively and no other additional peaks were observed.

Several factors including size, crystallinity, defects, and metal ion doping can influence the phase transition temperature but here the origin of elevated multiple T_C at higher temperature ($T_{C2\text{-heat}}$, $T_{C2\text{-cool}}$) can be attributed to the formation of M2 and M3 phases.[28] It was observed previously that these intermediate phases form stable local structure under high pressure or under stress/strain and consecutively increase the MIT temperature.[21,61,62] The increase in the V^{5+}:V^{4+} ratio (Table 1) was found to generate unrelaxed local strain to promote the formation of M2 and M3 phases.[41] At 550–600 °C the higher $T_{C2\text{-heat}}$

and $T_{C2\text{-cool}}$ was mainly due to M2 phase whereas at 700 °C, both M2 and M3 phases co-exist which also account for the slight red shift in $T_{C2\text{-heat}}$. It was also evident from SEM that high degree of morphological change in M2 and M2+M3 than M1 showing slightly preserved morphology. Thus, temperature induced strain was found to be essential for the stabilization of M2 and M3 phases. While the strain effect increases the T_C, annealing

Table 1. Binding energies (BE, eV) and V-ratios for the six VO$_2$ samples.

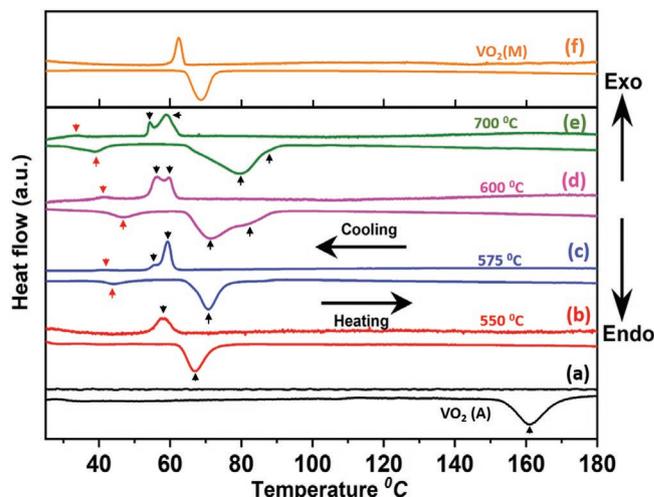| Sample	V(V) 2p$_{3/2}$ B.E/eV	V(IV) 2p$_{3/2}$ B.E/eV	V(III) 2p$_{3/2}$ B.E/eV	V(IV):V(V)	V(IV):V(III)
VO$_2$(A)	517.3	515.9	–	1.5	–
550 °C	517.3	515.5	–	0.3	–
575 °C	517.5	516.1	514.6	1.0	4.0
600 °C	517.5	516.1	514.7	0.6	3.0
700 °C	517.6	516.2	515.0	0.6	2.6
VO$_2$(M1)	517.6	516.2	–	1.7	–

Figure 6. DSC heating and cooling cycle of sample a) as-synthesized VO$_2$(A) followed by samples annealed at b) 550 °C, c) 575 °C, d) 600 °C, and e) 700 °C. f) Sample obtained after annealing at 570 °C under low vacuum (4 mbar).

**ADVANCED
SCIENCE NEWS**

www.advancedsciencenews.com

**ADVANCED
FUNCTIONAL
MATERIALS**

www.afm-journal.de

with decreased oxygen-flow of VO_2 induce oxygen vacancies that reduce the activation energy and suppress the critical temperature ($T_{C3-heat}$) by stabilizing the rutile phase.[22,57,63] In particular, the oxygen vacancies effectively influence the lattice structure by increasing electron concentration and form some lower valence V^{3+} ions, which destabilize the ordered V^{4+} chain structure by forming V^{3+}-V^{4+} pairs.[64,65] The formation of V^{3+} was observed through XPS analysis (Figure 5c–e). Hence, concentration of oxygen V^{3+} ions play crucial role in lowering the phase transition temperature. Thermal annealing with slightly increased oxygen content (vacuum 10–12 mbar) results in the formation of higher valence V_6O_{13} which reported to show negative T_C,[66] whereas thermal annealing at low vacuum derive the formation of pure M1 phase. These results establish the critical role of vacuum pressure during thermal annealing of the sample on the phase transformation as well as on the phase transition temperature. In addition, the distinct effect caused by strain and oxygen vacancy in the bulk VO_2 particles was observed in detail which has not been much reported in the literature and was mainly focused on thin-film materials. We should also note that, here the temperature induced strain on colloidal particles was not axial specific with those observed in the literature and strain imparted on the particles was uniform in all direction.

Tuning of T_C to near room temperature along with improved latent heat of phase transition found to be critical for energy saving performance in smart windows. In some cases, elemental doping of VO_2 was found to have a negative effect by lowering the latent heat of the phase transition and showing worse optical performance.[67] This is because as it has been observed, the solar energy modulation ability of VO_2—based composite films is nearly proportional to their latent heat.[68] Tables S2 and S3, Supporting Information summarizes the latent heat (ΔH) calculated from the area of the peak at each transition temperature (T_C) during heating and cooling cycles. Significant enhancement of latent heat ($\Delta H_1 + \Delta H_2)_{heat}$ was observed with increasing annealing temperature, which signifies improved crystallinity of the sample. The latent heat ($\Delta H_1 + \Delta H_2)_{heat}$ of 25.2 J g^{-1} at 550 °C increases to 50.8 J g^{-1} upon annealing at 600 °C which again slightly decreases to 46.4 J g^{-1} at 700 °C during IMT transition. This value is in comparison with the latent heat of 51 J g^{-1} which was reported for the bulk nanorods.[29,69] The slight drop in the latent heat at 700 °C can be attributed to the structural transformation from microrods to microspheres. A similar trend was observed in the calculated latent heat ($\Delta H_1 + \Delta H_2)_{cool}$ during MIT transition. VO_2(M1) sample obtained after annealing under low vacuum (4 mbar), showed latent heat of 56.3 and 27.8 J g^{-1} during heating and cooling cycle respectively. The difference in the latent heat during the heating and cooling cycle can be attributed to the change in the heating and cooling rate during the measurement (see Experimental Section). It should also be noted that stable reversibility was retained along with multiple T_C (Sample 600 °C) during multiple heating and cooling cycles of the sample (Figure S6, Supporting Information). Hence, the combined effect of oxygen vacancy as well as temperature induced strain not only cause the multiple lower and higher T_C, but also increases the crystallinity of the sample and improve the latent heat of phase transition.

3. Conclusion

Phase transformation of metastable VO_2(A) microrods was carried out across different annealing temperatures and vacuum to form high valence as well as intermediate insulating vanadium oxide phases. Thermal annealing under high (10–12 mbar), intermediate (7–9 mbar), and low vacuum (4 mbar) were shown to yield V_6O_{13}, VO_2(M2)/VO_2(M2+M3), and VO_2(M1) phase respectively. XRD and Raman spectroscopy measurements revealed the phase transformation sequence as (A)→(R)→(M2), (A)→(R)→(M2 + M3), and (A)→(R)→(M1).

Variation in the oxygen content and annealing temperature, were shown to substantiate a change in the multiple phase transition (T_C). Specifically, temperature induced stress and strain were found to facilitate the formation of intermediate M2 and M3 phases thus increasing the T_C from 66.8 to 79.5 °C. Whereas, oxygen vacancies in strain stabilized phase suppress the T_C to as low as 34.1 °C. Furthermore, annealed samples were found to possess high latent heat due to the increase in the crystallinity. To that end, this research provides a facile route to tune the electronic property of VO_2 colloidal particles by a simple thermal annealing process with varied oxygen content and additionally facilitates research into the role of strain/stress and oxygen vacancy over MIT.

4. Experimental Section

Vanadium pentoxide (V_2O_5, 99.6%), hydrazine hydrate solution ($N_2H_4 \cdot H_2O$, 85%), sulfuric acid (H_2SO_4, 95%), cetyl trimethy ammonium bromide (CTAB, 98%), sodium hydroxide (NaOH), ethanol (C_2H_5OH) were used without further purification.

Synthesis of Vanadium Oxide (VO_2) Nanowires: VO_2 nanowires were synthesized with a slightly modified procedure as reported earlier.[44] 0.45 g of V_2O_5 was dispersed in 15 mL of deionized water with continuous magnetic stirring to form a yellow suspension. 0.75 mL of H_2SO_4 was added while heating the suspension at 60 °C. Later, 0.27 mL of hydrazine hydrate $N_2H_2.H_2O$ was slowly added to the above mixture to form a transparent blue color indicating the reduction of V^{5+} to V^{4+}. With vigorous stirring, 0.08 mL of CTAB (0.1 M) was added and the solution kept stirring for 1 h. The pH of the resulting solution was then adjusted to 4.3–4.6 by adding NaOH (1 M) dropwise. The brown precipitate was washed with water and re-dispersed in 20 mL water and transferred to a 100 mL PPL lined Autoclave. Hydrothermal reaction was carried out at 230 °C degree for 63 h. The final black precipitate was collected by centrifugation, washed with ethanol and dried at 80 °C for 1h. Thermal transformation of VO_2(A) was carried out in vacuum tube furnace between 4–12 mbar at different annealing temperatures.

Sample Characterization: Morphology and size of the as-prepared VO_2 samples were obtained using a field emission scanning electron microscope, JEOL JSM-6701F instrument with an accelerating voltage of 5 KeV and transmission electron microscopy (TEM) analysis was performed using a JEM2100 TEM, operated at 200 kV. The crystallographic phase identification of VO_2 samples and phase transformation with temperature were determined by STOE SEIFERT diffractometer with angular range of 2° < 2θ < 45° and by using Mo K-alpha X-ray radiation source. In situ PXRD measurements were carried out on a Stoe STADI-P instrument using Mo K-alpha X-ray radiation source with a wavelength of 0.7093 Å. The 2θ range was 2–40° at a step size of 0.495° and time of 0.5 s per step. The samples were packed into 0.5 mm quartz glass capillary and the top sealed using vacuum grease to minimize sample oxidation during heating. Measurements were taken initially at 25 °C followed by measurements from 400–700 °C with 25 °C intervals and from 700–25 °C at 25 °C intervals. Raman spectra were recorded in back

**ADVANCED
SCIENCE NEWS**
www.advancedsciencenews.com

**ADVANCED
FUNCTIONAL
MATERIALS**
www.afm-journal.de

scattering geometry using 532 nm excitation in Renishaw inVia confocal microscope. Spectra were collected over 60 s scans by using 0.1% laser power to minimize sample oxidation. Elemental analysis was performed by using XRF (Epsilon 4 Malvern Panalytical) with an accuracy limit to as low as 10 ppm. XPS was carried out on a Thermo Scientific K-alpha photoelectron spectrometer with a dual beam charge compensation system using monochromatic Al$_{k\alpha}$ radiation. High-resolution scans were recorded for the principal peaks of C (1s), V (2p), and O (1s) at a pass energy of 50 eV. The binding energies were calibrated with respects to O1s peak at 530.0 eV. All peak fittings were carried out using CasaXPS software. DSC analysis was performed on a DSC instrument from Mettler Toledo, where experiments were carried out between 25 to 200 °C under nitrogen atmosphere with a heating rate of 5 °C min^{-1}.

This instrument does not have cooling setup and will cool down at the natural cooling rate. The cooling rate was approximated with each segment and the cooling rate was set to 0.5 °C min^{-1} and the latent heat was calculated. Therefore, there was a slight difference between the latent heat in the heating and cooling cycle.

Supporting Information

Supporting Information is available from the Wiley Online Library or from the author.

Conflict of interest

The authors declare no conflict of interest.

[1] L. A. Ladd, W. Paul, *Solid State Commun.* **1969**, *7*, 425.
[2] J. B. Goodenough, *J. Solid State Chem.* **1971**, *3*, 490.
[3] K. Liu, S. Lee, S. Yang, O. Delaire, J. Wu, *Mater. Today* **2018**, *21*, 875.
[4] M. F. Jager, C. Ott, P. M. Kraus, C. J. Kaplan, W. Pouse, R. E. Marvel, R. F. Haglund, D. M. Neumark, S. R. Leone, *Proc. Nat. Acad. Sci. U. S. A.* **2017**, *114*, 9558.
[5] M. Nakano, K. Shibuya, D. Okuyama, T. Hatano, S. Ono, M. Kawasaki, Y. Iwasa, Y. Tokura, *Nature* **2012**, *487*, 459.
[6] G. Stefanovich, A. Pergament, D. Stefanovich, *J. Phys. Condens. Matter* **2000**, *12*, 8837.
[7] Y. Ke, C. Zhou, Y. Zhou, S. Wang, S. H. Chan, Y. Long, *Adv. Funct. Mater.* **2018**, *28*, 1800113.
[8] H. N. Kim, S. Yang, *Adv. Funct. Mater.* **2019**, *1902597*, 1.
[9] T. D. Manning, I. P. Parkin, M. E. Pemble, D. Sheel, D. Vernardou, *Chem. Mater.* **2004**, *16*, 744.
[10] J. Li, W. Liu, X. Zhang, P. K. Chu, K. M. C. Cheung, K. W. K. Yeung, *Mater. Today* **2019**, *22*, 35.
[11] N. Manca, L. Pellegrino, T. Kanki, W. J. Venstra, G. Mattoni, Y. Higuchi, H. Tanaka, A. D. Caviglia, D. Marré, *Adv. Mater.* **2017**, *29*, 1701618.
[12] S. E. Zaki, M. A. Basyooni, M. Shaban, M. Rabia, Y. R. Eker, G. F. Attia, M. Yilmaz, A. M. Ahmed, *Sensors Actuators, A Phys.* **2019**, *294*, 17.
[13] B. Hu, Y. Ding, W. Chen, D. Kulkarni, Y. Shen, V. V. Tsukruk, Z. L. Wang, *Adv. Mater.* **2010**, *22*, 5134.
[14] G. P. Evans, M. J. Powell, I. D. Johnson, D. P. Howard, D. Bauer, J. A. Darr, I. P. Parkin, *Sensors Actuators, B Chem.* **2018**, *255*, 1119.
[15] M. Li, S. Magdassi, Y. Gao, Y. Long, *Small* **2017**, *13*, 1701147.
[16] Z. Song, L. Zhang, F. Xia, N. A. S. Webster, J. Song, B. Liu, H. Luo, Y. Gao, *Inorg. Chem. Front.* **2016**, *3*, 1035.
[17] S. Rao Popuri, A. Artemenko, C. Labrugere, M. Miclau, A. Villesuzanne, M. Pollet, *J. Solid State Chem.* **2014**, *213*, 79.
[18] S. Zhang, B. Shang, J. Yang, W. Yan, S. Wei, Y. Xie, *Phys. Chem. Chem. Phys.* **2011**, *13*, 15873.
[19] L. Zhang, J. Yao, Y. Guo, F. Xia, Y. Cui, B. Liu, Y. Gao, *Ceram. Int.* **2018**, *44*, 19301.
[20] S. Y. Li, G. A. Niklasson, C. G. Granqvist, *Thin Solid Films* **2012**, *520*, 3823.
[21] H. Kim, T. V. Slusar, D. Wulferding, I. Yang, J. C. Cho, M. Lee, H. C. Choi, Y. H. Jeong, H. T. Kim, J. Kim, *Appl. Phys. Lett.* **2016**, *109*.
[22] J. Jeong, N. Aetukuri, T. Graf, T. D. Schladt, M. G. Samant, S. S. P. Parkin, *Science* **2013**, *339*, 1402.
[23] Y. Chen, Z. Wang, S. Chen, H. Ren, L. Wang, G. Zhang, Y. Lu, J. Jiang, C. Zou, Y. Luo, *Nat. Commun.* **2018**, *9*, 818.
[24] C. Marini, E. Arcangeletti, D. Di Castro, L. Baldassare, A. Perucchi, S. Lupi, L. Malavasi, L. Boeri, E. Pomjakushina, K. Conder, P. Postorino, *Phys. Rev. B* **2008**, *77*, 235111.
[25] G. Villeneuve, M. Drillon, P. Hagenmuller, M. Nygren, J. P. Pouget, F. Carmona, P. Delhaes, *J. Phys. C, Solid State Phys.* **1977**, *10*, 3621.
[26] M. Marezio, *Phys. Rev. B* **1972**, *91*.
[27] P. M. Herdiana, *Phys. Rev. Lett.* **1975**, *35*, 873.
[28] J. H. Park, J. M. Coy, T. Serkan Kasirga, C. Huang, Z. Fei, S. Hunter, D. H. Cobden, *Nature* **2013**, *500*, 431.
[29] J. Cao, Y. Gu, W. Fan, L. Q. Chen, D. F. Ogletree, K. Chen, N. Tamura, M. Kunz, C. Barrett, J. Seidel, J. Wu, *Nano Lett.* **2010**, *10*, 2667.
[30] H. Guo, K. Chen, Y. Oh, K. Wang, C. Dejoie, S. A. Syed Asif, O. L. Warren, Z. W. Shan, J. Wu, A. M. Minor, *Nano Lett.* **2011**, *11*, 3207.
[31] Z. Shao, X. Cao, H. Luo, P. Jin, *NPG Asia Mater.* **2018**, *10*, 581.
[32] N. B. Aetukuri, A. X. Gray, M. Drouard, M. Cossale, L. Gao, A. H. Reid, R. Kukreja, H. Ohldag, C. A. Jenkins, E. Arenholz, K. P. Roche, H. A. Dürr, M. G. Samant, S. S. P. Parkin, *Nat. Phys.* **2013**, *9*, 661.
[33] S. Kittiwatanakul, S. A. Wolf, J. Lu, *Appl. Phys. Lett.* **2014**, *105*, 073112.
[34] J. Cao, E. Ertekin, V. Srinivasan, W. Fan, S. Huang, H. Zheng, J. W. L. Yim, D. R. Khanal, D. F. Ogletree, J. C. Grossman, J. Wu, *Nat. Nanotechnol.* **2009**, *4*, 732.
[35] Y. Muraoka, Z. Hiroi, *Appl. Phys. Lett.* **2002**, *80*, 583.
[36] V. Eyert, *Ann. der Phys.* **2002**, *11*, 650.
[37] H. Qiu, M. Yang, Y. Dong, H. Xu, B. Hong, Y. Gu, Y. Yang, C. Zou, Z. Luo, C. Gao, *New J. Phys.* **2015**, *17*, 113016.
[38] J. P. T. M. Rice, H. Launois, *Phys. Rev. Lett.* **1994**, *73*, 3042.
[39] T. Kanki, H. Takami, S. Ueda, A. N. Hattori, K. Hattori, H. Daimon, K. Kobayashi, H. Tanaka, *Phys. Rev. B* **2011**, *84*, 085107.
[40] L. L. Fan, S. Chen, Z. L. Luo, Q. H. Liu, Y. F. Wu, L. Song, D. X. Ji, P. Wang, W. S. Chu, C. Gao, C. W. Zou, Z. Y. Wu, *Nano Lett.* **2014**, *14*, 4036.

ADVANCED
SCIENCE NEWS

www.advancedsciencenews.com

ADVANCED
FUNCTIONAL
MATERIALS

www.afm-journal.de

[41] J. Zhang, Z. Zhao, J. Li, H. Jin, F. Rehman, P. Chen, Y. Jiang, C. Chen, M. Cao, Y. Zhao, *ACS Appl. Mater. Interfaces* **2017**, *9*, 27135.

[42] R. Basu, M. Sardar, S. Bera, P. Magudapathy, S. Dhara, *Nanoscale* **2017**, *9*, 6537.

[43] J. Zhang, H. Jin, Z. Chen, M. Cao, P. Chen, Y. Dou, Y. Zhao, J. Li, *Chem. Mater.* **2015**, *27*, 7419.

[44] J. H. Son, J. Wei, D. Cobden, G. Cao, Y. Xia, *Chem. Mater.* **2010**, *22*, 3043.

[45] J. Hou, J. Zhang, Z. Wang, Z. Zhang, Z. Ding, *RSC Adv.* **2014**, *4*, 18055.

[46] P. Shvets, O. Dikaya, K. Maksimova, A. Goikhman, *J. Raman Spectrosc.* **2019**, *50*, 1226.

[47] H. Y. Xu, K. W. Xu, F. Ma, P. K. Chu, *RSC Adv.* **2018**, *8*, 10064.

[48] B. L. Chamberland, *J. Solid State Chem.* **1973**, *7*, 377.

[49] K. D. Rogers, *Powder Diffr.* **1993**, *8*, 240.

[50] T. J. Huffman, C. Hendriks, E. J. Walter, J. Yoon, H. Ju, R. Smith, G. L. Carr, H. Krakauer, M. M. Qazilbash, *Phys. Rev. B* **2017**, *95*, 075125.

[51] J. M. Atkin, S. Berweger, E. K. Chavez, M. B. Raschke, J. Cao, W. Fan, J. Wu, *Phys. Rev. B* **2012**, *85*, 020101.

[52] S. Zhang, I. S. Kim, L. J. Lauhon, *Nano Lett.* **2011**, *11*, 1443.

[53] B. Dong, N. Shen, C. Cao, Z. Chen, H. Luo, Y. Gao, *RSC Adv.* **2016**, *6*, 81559.

[54] G. Silversmit, D. Depla, H. Poelman, G. B. Marin, R. De Gryse, *J. Electron Spectrosc. Relat. Phenomena* **2004**, *135*, 167.

[55] J. Mendialdua, R. Casanova, Y. Barbaux, *J. Electron Spectrosc. Relat. Phenomena* **1995**, *71*, 249.

[56] M. C. Biesinger, L. W. M. Lau, A. R. Gerson, R. S. C. Smart, *Appl. Surf. Sci.* **2010**, *257*, 887.

[57] Z. Zhang, Y. Gao, Z. Chen, J. Du, C. Cao, L. Kang, H. Luo, *Langmuir* **2010**, *26*, 10738.

[58] D. Guo, Z. Zhao, J. Li, J. Zhang, R. Zhang, Z. Wang, P. Chen, Y. Zhao, Z. Chen, H. Jin, *Cryst. Growth Des.* **2017**, *17*, 5838.

[59] S. R. Popuri, A. Artemenko, R. Decourt, A. Villesuzanne, M. Pollet, *Phys. Chem. Chem. Phys.* **2017**, *19*, 6601.

[60] Y. Oka, S. Sato, T. Yao, N. Yamamoto, *J. Solid State Chem.* **1998**, *141*, 594.

[61] B. Dong, N. Shen, C. Cao, Z. Chen, H. Luo, Y. Gao, *RSC Adv.* **2016**, *6*, 50521.

[62] Y. Chen, S. Zhang, F. Ke, C. Ko, S. Lee, K. Liu, B. Chen, J. W. Ager, R. Jeanloz, V. Eyert, J. Wu, *Nano Lett.* **2017**, *17*, 2512.

[63] C. H. Griffiths, H. K. Eastwood, *J. Appl. Phys.* **1974**, *45*, 2201.

[64] J. B. C. C. Tang, P. Georgopoulos, M. E. Fine, *Phys. Rev. B* **1985**, *31*, 1000.

[65] Z. Zhang, F. Zuo, C. Wan, A. Dutta, J. Kim, J. Rensberg, R. Nawrodt, H. H. Park, T. J. Larrabee, X. Guan, Y. Zhou, S. M. Prokes, C. Ronning, V. M. Shalaev, A. Boltasseva, M. A. Kats, S. Ramanathan, *Phys. Rev. Appl.* **2017**, *7*, 034008.

[66] R. Bloch, B. Tess, *Mat. Res. Bull.* **1974**, *1*, 11.

[67] W. Li, S. Ji, Y. Li, A. Huang, H. Luo, P. Jin, *RSC Adv.* **2014**, *4*, 13026.

[68] J. Zou, X. Chen, L. Xiao, *Mater. Res. Express* **2018**, *5*.

[69] C. N. Berglund, H. J. Guggenheim, *Phys. Rev.* **1969**, *185*, 1022.